

Effect of Disorder and Doping on Electronic Structure and Diffusion Properties of $\text{Li}_3\text{V}_2\text{O}_5$

Mohammad Babar, Hasnain Hafiz, Zeeshan Ahmad, Bernardo Barbiellini, Arun Bansil, and Venkatasubramanian Viswanathan*



Cite This: *J. Phys. Chem. C* 2022, 126, 15549–15557



Read Online

ACCESS |



Metrics & More

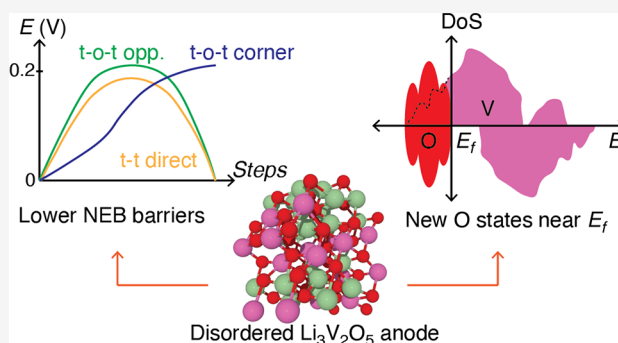


Article Recommendations



Supporting Information

ABSTRACT: V_2O_5 in its ω phase ($\text{Li}_3\text{V}_2\text{O}_5$) with excess lithium is a potential alternative to the graphite anode for lithium-ion batteries at low temperature and fast charging conditions owing to its safer voltage (0.6 V vs $\text{Li}^+/\text{Li(s)}$) and high lithium transport rate. In-operando cationic disorder, as observed in most ordered materials, can produce significant changes in charge compensation mechanisms, anionic activity, lithium diffusion, and operational voltages. In this work, we report the variation in structural distortion, electronic structure, and migration barrier accompanied by disorder using first-principles calculations. Owing to the segregation of lithium atoms in the disordered state, we observe greater distortion, emergence of metallic behavior, and potential anionic activity from nonbonding oxygen states near the Fermi level. Redox capacity can be tuned by doping with 3d metals, which can adjust the participating cationic states, and by fluorine substitution, which can stabilize or suppress anionic states. Moreover, the suppression of anionic activity is found to decrease structural distortion, which is crucial for mitigating voltage fade and hysteresis. Diffusion barrier calculations in the presence of disorder indicate the activation of the remaining 3D paths for lithium hopping which are unavailable in the ordered configuration, explaining its fast-charging ability observed in experiments.



INTRODUCTION

The high capacity and long cycle life of lithium-ion batteries form the dominant characteristics for both near-term and long-term technologies in consumer electric vehicles and aviation, aerospace, and energy storage devices.^{1–3} Transition metal oxides (TMOs) with disordered rock salt (DRS) structure, e.g., $\text{Li}_2\text{W}_2\text{O}_7$, Li_2MoO_4 , Li_2NbO_4 , and $\text{Li}_2\text{VO}_2\text{F}$, have been a popular choice for high-capacity lithium-rich positive electrode (cathodes) materials.^{4–7} Out of these, lithium vanadium pentaoxide ($\text{Li}_x\text{V}_2\text{O}_5$) has been under critical examination for more than 30 years since first proposed.⁸ Structurally significant phases in V_2O_5 have been accurately determined experimentally⁹ starting from the layered α , ϵ , δ , and γ phases to the fully reduced DRS ω phase for $x = 3$ in $\text{Li}_x\text{V}_2\text{O}_5$. As a cathode, the layered phases are reversible, have an acceptable voltage range (2–4 V), and undergo small volume expansion.^{9,10} Nanostructure engineering of V_2O_5 to improve these properties has also shown significant enhancement in cathodic performance.^{11–14} More recently, however, Liu et al.¹⁵ showed that excess lithium insertion in V_2O_5 in its ω phase ($x = 3–5$) is also reversible and can be used as a fast-charging anode. Its average operational voltage is 0.4 V higher than that of graphite (0.2 V vs $\text{Li}^+/\text{Li(s)}$), i.e., a broader potential range for lithium insertion offering better stability

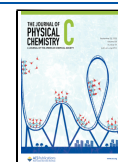
and safety against plating under low-temperature and fast-charging conditions.^{16–18} Consequently, the irreversible transformation from layered to DRS ($\gamma\text{--}\omega$) marks the fully lithiated (delithiated) phase as a cathode (anode).

Starting with the ordered structure, operational temperature and voltage fluctuations during charge–discharge cycles can potentially cause in-operando cationic disorder.¹⁹ This is commonly accompanied by structural distortions and activation of alternate reaction centers like anionic redox, which can change the electrode capacity and cause detrimental effects like hysteresis, voltage fade, and sluggish kinetics.²⁰ Oxygen redox can happen at voltages as low as 3.0 V in Li_2O .²¹ Therefore, contrary to the norm that anionic activity is limited to cathodes, we might observe disorder-mediated oxygen redox in a lithium excess $\text{Li}_{3+x}\text{V}_2\text{O}_5$ anode, mainly during the initial stages of lithium insertion ($x \ll 1$). The electronic structure of pristine $\text{Li}_3\text{V}_2\text{O}_5$ can highlight important differences in reaction

Received: May 13, 2022

Revised: August 5, 2022

Published: September 12, 2022



mechanisms of disordered and ordered systems. Moreover, these differences can be engineered with the doping of anions (e.g., fluorination) and cations (transition metal substitution) within the bulk. Anionic substitution by fluorine is known to increase the cationic redox capacity,^{4,21} while 3d metal substitution can modulate the activity of either redox center. There is also a greater possibility for easier microscopic diffusion in the disorder owing to the formation of favorable cation clusters relevant to lithium transport^{22,23} and smaller hindrance by distortion. Macroscopic diffusion paths are already activated by a connected percolation network of OTM sites when lithium excess is above a threshold in the disorder.^{23,24}

Here, we present a first-principles comparison of the electronic structure between the pristine ordered and disordered $\text{Li}_3\text{V}_2\text{O}_5$ and its correlation with structural distortion, for better insight into the effects of cationic disorder. We obtain the reference (ordered and disordered) structures by sorting the configurations on the basis of the formation energies and electron population in oxygen atoms as descriptors. We assume the reference structures to be representative of the ordered and disordered regimes in $\text{Li}_3\text{V}_2\text{O}_5$. Using normal coordinates,²⁵ we transform displacement errors of the most disfigured octahedron into distortion modes (stretching, bending, twisting, etc.), allowing better quantification of structural distortion induced by disorder and doping. Next, we employ projected density of states (pDOS) obtained from density functional theory (DFT) calculations to analyze the nature of oxygen bonding and their locations with respect to the Fermi level and transition metal (TM) states, in ordered, disordered, and doped structures. Potential peroxo bonds between oxygen atoms are examined via crystal orbital/Hamiltonian overlap population (COOP/COHP) calculations. A consistent correlation between the structural distortion and the activity of anionic centers in the disordered structure is observed, which can be suppressed or enhanced with cationic (3d metal) or anionic (fluorine) doping. Finally, the possibility for improved microscopic diffusion due to weakening TM–O bonds in the disordered state is investigated using nudged elastic band (NEB) calculations. This enables us to study the effect of disorder on the electronic structure and microscopic diffusion of $\text{Li}_3\text{V}_2\text{O}_5$ within an ab initio framework. Our study could be an important step toward exploiting the strengths of disordered systems while mitigating voltage fade and structural degradation.

METHODS

All DFT calculations were performed using the Quantum Espresso (QE)²⁶ code with Ultrasoft pseudopotentials.²⁷ We employed the Perdew–Burke–Ernzerhof (PBE)²⁸ generalized gradient approximation (GGA) exchange correlation functional with a Hubbard U extension of 3.25 eV^{15,29} on the vanadium site for obtaining energies, atomic relaxations, electronic structure, and migration barriers. It is well-known that GGA+ U and hybrid functional methods have a qualitatively equivalent behavior in transition metal complexes (TMCs).³⁰ Previous first-principles studies^{29,31} demonstrated that GGA+ U can essentially capture accurate electronic structures in vanadate-based oxides. Liu et al.¹⁵ also reported that the GGA+ U approach could achieve a qualitatively accurate open-circuit voltage (OCV) trend, subphase transitions, and volume changes in $\text{Li}_{3+x}\text{V}_2\text{O}_5$ matching with experiments.

For other 3d metals, U values fitted from binary formation enthalpies have been taken from Jain et al.³² The kinetic energy cutoff for plane waves and the charge density were fixed at 544 eV (40 Ry) and 5440 eV (400 Ry), respectively.¹⁵ All systems were initialized with a high-spin ferromagnetic configuration for the least error in relative energies.³³ The energies and forces were converged to 0.0013 eV (10^{-4} Ryd) per cell and 0.0257 eV/Å (10^{-3} Ry/Bohr), respectively. All relaxations were performed using Broyden–Fletcher–Goldfarb–Shanno (BFGS) optimization.³⁴ Crystal orbital overlap populations (COOP) were obtained using the LOBSTER code³⁵ for an analysis of the O–O and V–O bond strengths, as performed earlier on other Li-TMOs.³⁶ A full set of symmetrically distinct orderings (80) of the same stoichiometry ($\text{Li}_3\text{V}_2\text{O}_5$) were generated using enumlib wrapper³⁷ to compare the cationic disorders.

The site occupancy of lithium atoms (tetrahedral or octahedral) was determined using the atomic simulation environment's (ASE)³⁸ Neighborlist functionality and Brunner's algorithm in pymatgen.³⁹ Lithium atoms with fourfold coordination are classified as tetrahedral sites and the five-coordinated square-pyramidal and six-coordinated octahedral environments as octahedral sites. For migration barriers, we used climbing image NEB with five transition steps. Supercells ($2 \times 2 \times 2$) of the single formula unit cell ($\text{Li}_3\text{V}_2\text{O}_5$) were chosen with approximately uniform and large enough ($\sim 9 \text{ Å} \times 9 \text{ Å} \times 9 \text{ Å}$) dimensions to avoid interactions with periodic images. Notably, we study the intensive properties of this material, which are unaffected by the less favorable higher energy orderings accessible in bigger supercells. We considered three types of lithium migration mechanisms, direct tetrahedron-to-tetrahedron (t-t) and intermediate octahedra knock-off at a corner site (t-o-t corner-sharing) or at opposite sites (t-o-t opposing).¹⁵ The energies and forces were converged to 0.0013 eV (10^{-4} Ryd) per cell and 0.0257 eV/Å (10^{-3} Ryd/Bohr), respectively.

For quantification of the structural distortion,²⁵ the displacement error between an ideal octahedron (O) and a disordered one (D) was transformed into normal modes as

$$D = O + \sum_i c_i \tilde{Q}_i \quad (1)$$

where c_i are mode coefficients and \tilde{Q}_i are normalized normal coordinates. The magnitude of the coefficients is indicative of the amount of distortion in a given mode. To get the displacement vectors ($D - O$), O is transformed with a 3D rotation matrix (yaw, pitch, and roll), which minimizes the displacement error under BFGS optimization. The ideal octahedron is assumed to have a uniform cubic parameter, experimentally observed from DRS- $\text{Li}_3\text{V}_2\text{O}_5$ (4.095 Å).¹⁵

RESULTS AND DISCUSSION

Disorder Formation Energies and Electron Population in Oxygen Atoms. The extent of cationic disorder in $\text{Li}_3\text{V}_2\text{O}_5$ can be organized by its formation energy and bonding character of oxygen atoms. From Figure 1, we observe that the formation energies vary almost linearly with the average population of electrons in oxygen 2p orbitals. Because stable configurations have a higher electron population, we can deduce that oxygen atoms approach the O^{2-} state in lower energy disorders owing to greater electron sharing by vanadium. Stronger covalent bonding by a mixed cationic

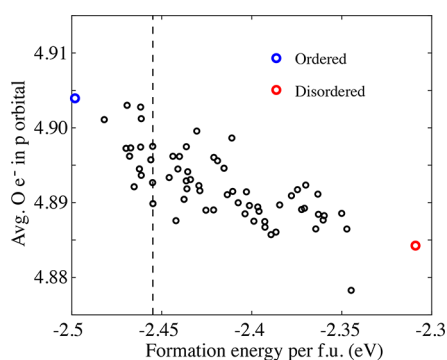


Figure 1. Formation energy per formula unit of the disordered configurations as a function of the average population of electrons in the oxygen p orbitals. Oxygen atoms digress from the full octet (O^{2-}) state with increasing extent of disorder and structural distortion. The stability of the configurations falls almost linearly with the average occupation of oxygen states. The edge points on either side, i.e., ordered (blue) and disordered (red) structures, are marked to be used as references for comparison. Structures on the left of the dashed line are accessible via configurational entropy at room temperature.

environment allows an ideal octahedron geometry around oxygen atoms with almost equal bond lengths and perpendicular angles. In contrast, structures with fewer electrons in the oxygen p shell mimic a peroxo-type state and are characterized by reduced stability and higher octahedral distortion. Therefore, the average electron population in anions can be used as a descriptor for the stability analysis of disordered configurations. To compare the order and disorder, we have chosen the edge points with the highest and lowest formation energies, respectively, as marked in Figure 1. Corresponding to these points, supercells containing eight formula units of $\text{Li}_3\text{V}_2\text{O}_5$ (Figure 2) were used as reference systems for further calculations. We assume the properties of in-between configurations to be intermediate of that of the edge points. All the configurations contain fully

filled octahedral sites (0.6:0.4 ratio of Li:V) and unreserved tetrahedral sites that allow additional lithium insertion. The formation energy per formula unit is given by

$$E_{\text{formation}} = E_{\text{Li}_x\text{V}_2\text{O}_5} - xE_{\text{Li(s)}} - 2E_{\text{V}} - \frac{5}{2}E_{\text{O}_2} \quad (2)$$

where $E_{\text{Li(s)}}$, E_{V} , and E_{O_2} are the DFT-calculated energies of standard lithium (bcc), vanadium (cubic), and oxygen clusters from Materials Project.⁴⁰

Figure 1 shows that the most ordered (leftmost) structure has a considerable energy gap with the rest of the structures, indicating a finite amount of short-range order in this configuration. At room temperature, however, more disorders can have energies close to the ordered structure owing to the configurational entropy from cationic rearrangement ($H - TS$).⁴¹ The dashed line marks the boundary on the left of which structures are thermodynamically accessible from configurational entropy at room temperature. Temperature fluctuations during charge–discharge cycles could further increase the disorder, resulting in higher formation energies.

Nearest-neighbor environments of tetrahedral sites are more uniform in the ordered system, allowing minimal segregation into Li_4 (OTM) tetrahedrons because electrostatic attraction of $\text{V}^{3.5+}$ with Li^+ dominates over the opposing size effect.²³ The mismatch in size between vanadium (0.78 \AA^{42}) and lithium (0.76 \AA^{23}) ions is small, allowing lesser strain with mixed Li–V tetrahedrons and thus increasing the energy to segregate. As expected, higher energy disorders have a greater concentration of OTM tetrahedrons.

Octahedral distortion at each anionic site can be quantified by transforming the displacement vectors of the neighbors from their ideal positions into orthogonalized normal coordinates decomposing them toward recognizable modes.²⁵ Consequently, each octahedron has 21 normal coordinates (7 atomic positions), whose coefficients are grouped into symmetric, asymmetric stretching, bending, twisting modes, etc., as given by Urban et al.²⁵ Table 1 compares the L2 norm

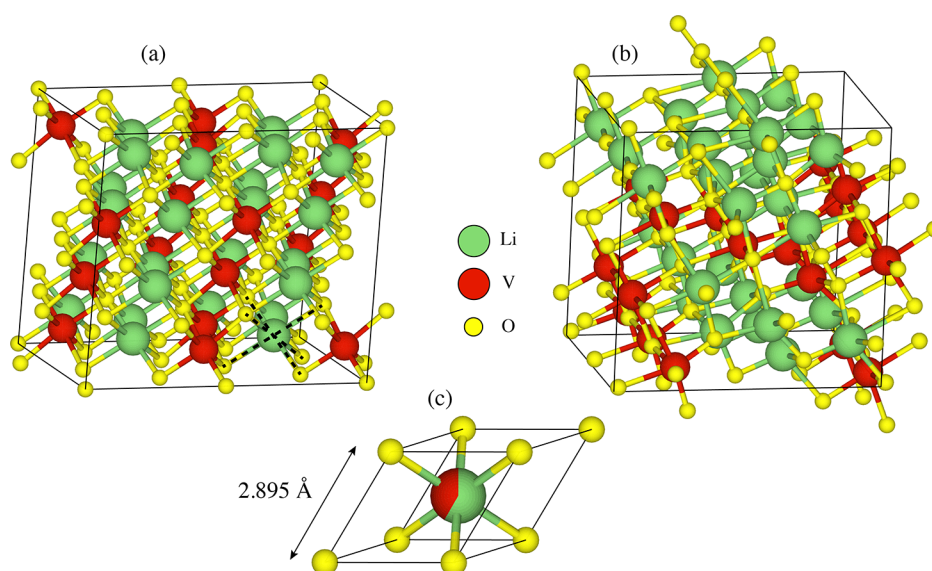


Figure 2. Supercells of ordered (left) and disordered (right) configurations corresponding to lowest and highest formation energies, respectively. Both contain 8 formula units (80 atoms) of $\text{Li}_3\text{V}_2\text{O}_5$, large enough to avoid adjacent image interactions. The ordered system has lithium atoms placed at periodic locations within the supercell, and anionic octahedrons are close to the ideal geometry with mixed Li/V neighbors. The disordered system has irregularly placed lithium with high structural distortion and segregated lithium (OLi_6) octahedrons.

Table 1. Normal (Symmetrical Stretching, Asymmetrical Stretching, Bending, Twisting, and Displacement) Mode Coefficients of the Most Distorted Anion Atom in the Ordered, Disordered, and (Two Anion and Two Cation) Doped Systems^a

system	c norm	sym. stretch	asym. stretch	bend	twist	displ.
ord. $\text{Li}_3\text{V}_2\text{O}_5$	0.547	0.0652	0.374	0.220	0.226	0.248
dis. $\text{Li}_3\text{V}_2\text{O}_5$	1.676	0.289	0.640	0.693	0.968	0.725
dis. $\text{Li}_3\text{V}_2\text{O}_4\text{F}(1)$	2.043	0.324	0.843	0.757	1.175	0.887
dis. $\text{Li}_3\text{V}_2\text{O}_4\text{F}(2)$	0.696	0.141	0.176	0.285	0.399	0.321
dis. Li_3TiVO_5	1.621	0.050	0.323	0.877	0.447	0.715
dis. Li_3NiVO_5	2.376	0.008	0.454	0.751	0.462	0.939

^aCombined L2 norms $\left(\sqrt{\sum_{i=1}^{21} c_i^2}\right)$ of all the modes are listed as column c norm.

of coefficients in different modes for the most distorted octahedron in ordered, disordered, and doped systems, respectively. Clearly, the ordered system has a much lower magnitude of coefficients than its counterpart across all modes. The higher distortion in disordered systems is responsible for hysteresis and greater chances of irreversible structural transformation.²⁰

Electronic Structure. The configuration of the nearest neighbors plays an important role in determining the contribution of oxygen in $\text{M}-\text{O}^*$ states in the electronic structure.^{20,43} Projected DOS for the ordered and disordered systems are shown in Figure 3. Unlike its counterpart, the ordered system seems almost insulating owing to the lack of states near the Fermi level, which could hinder lithium transport. The disorder shows a metallic behavior, better for fast-charging applications. We shall investigate lithium transport differences more in the Migration Barriers section.

In the ordered system, we have a mixed $\text{Li}-\text{V}$ environment in which none of the oxygen atoms forms an OLi_6 octahedron. As expected, we observe delocalized 2p oxygen states in its pDOS (Figure 3a).⁴³ Consequently, we anticipate negligible anionic redox in the ordered configuration owing to the absence of redox-active nonbonding states in oxygen atoms. In contrast, the disordered configuration has a variety of nearest-neighbor environments. Owing to lithium segregation, we can identify OLi_6 octahedrons in the unit cell, from which we

expect nonbonding 2p oxygen states to arise near the Fermi level. This character is reflected in the pDOS of oxygen (Figure 3b) near the Fermi level. One of the important descriptors of reversible anionic redox is the presence of both transition metal and anion states around the Fermi level for electron extraction during the delithiation process.²⁰ More specifically, the nonbonding oxygen 2p orbitals must be partially filled near the Fermi level to facilitate electron addition to these states. As lithium is introduced, these 2p states get filled and shift deeper below the Fermi level, as identified for Li_2RuO_3 .³⁶ However, we find limited participation of these nonbonding oxygen states in the disordered structures where these states are already filled and stay below the Fermi level.

In Figure S1, the crystal orbital overlap population (COOP) of O–O bonds in the pristine disorder is similar in magnitude to the ordered structure. The average oxygen bond length is also shorter (2.55 vs 2.69 Å). To test if the partial O–O bonds in the disorder participate in the redox, we sequentially inserted (and relaxed) two lithium atoms ($x = 0.125$) in energetically favorable tetrahedral sites and observed the O–O bond COOP magnitudes. As evident in Figure S2, the overlap populations do not change significantly, which is in contrast with the drastic suppression of O–O COOP in LiRuO_3 vs RuO_3 ,³⁶ where electrons fill the empty 2p states, subsequently breaking peroxo O–O bonds upon lithium insertion. On the basis of the pDOS and COOP analysis, we conclude that the unhybridized oxygen states in the disordered system are not destabilized enough to participate in the redox at 0 K. However, these states are close enough to get activated at higher temperatures, with voltage fluctuations that shift the Fermi level, and result in surface densification^{20,44} during charge–discharge cycles. We expect a similar trend to hold in other disordered configurations lying at intermediate energies (see Figure 1).

Another way to engineer the activity of redox centers is through cationic and anionic substitution, which we explore next. We shall investigate the effect of doping on the electronic structure in terms of the newly introduced redox-active states as well as the accompanied change in structural distortion. We study the electronic structure change due to anionic substitution by fluorine and cationic substitution by 3d transition metals. Fluorine, being a more electronegative species than oxygen, decreases the average anionic charge and increases the metal redox capacity in TMOs.²¹

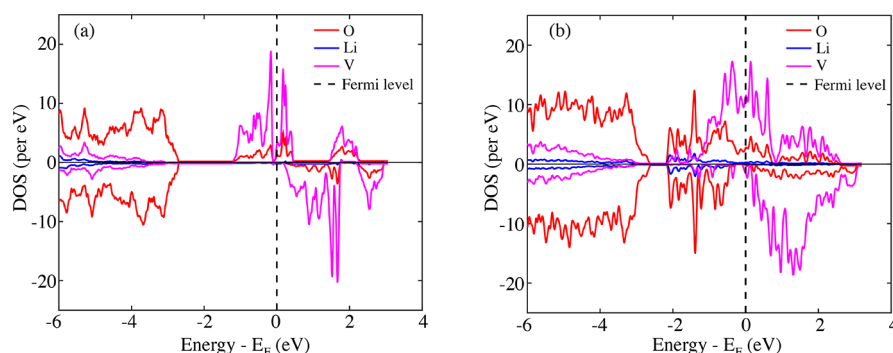


Figure 3. Atom-projected density of states of the ordered (a) and disordered (b) configurations. The disordered structure has mostly filled unhybridized oxygen states (spikes) near the Fermi level (E_F), caused by oxygen atoms surrounded by lithium only. The mixed Li/V octahedral environment in the ordered system increases covalent sharing with oxygen and delocalizes its states to lower energies. Consequently, the average population in oxygen p orbitals is lower in the disordered system because some nonbonding states are unfilled near the Fermi level.

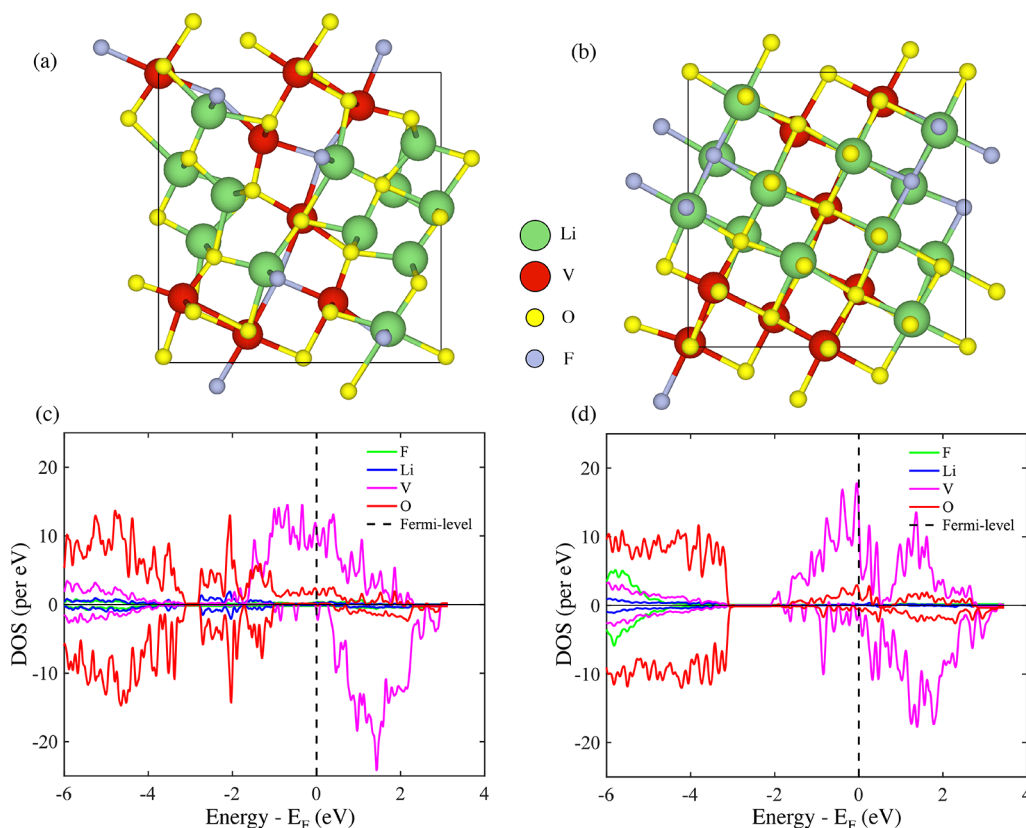


Figure 4. Atom-projected density of states for the two cases of fluorinated-disordered $\text{Li}_3\text{V}_2\text{O}_4\text{F}$ systems. Cation-mixed fluorine (a) maintains octahedral distortion and pushes unhybridized 2p oxygen states deeper into the Fermi level (c). When fluorine occupies sites with an all-lithium environment, distortion is reduced (b) and all oxygen nonbonding states are suppressed near the Fermi level (d). Owing to high electron affinity, nonbonding fluorine states occur at much lower energies, which are visible as increased DOS magnitude around -6 eV in (d).

Effect of Fluorination. The partial fluorine substitution of oxygen atoms can stabilize or suppress anionic states to allow greater cationic redox and reduce anion participation under thermodynamic activation (high temperature, voltage fluctuations, etc.). Previous works have shown a high increase in capacity via fluorine substitution of manganese-based TM oxides (>300 mAh g^{-1}).²¹ With vanadium, the capacity increase has been reported to be higher, from 295 mAh g^{-1} in Li_2VO_3 to 420 mAh g^{-1} in $\text{Li}_2\text{VO}_2\text{F}$.^{4,21} The presence of vanadium as a high-valent, redox-active TM also supports charge compensation on the cation and reduces anionic activity.⁴⁵ To understand this effect, we prepared two fluorine-doped structures of the disordered system replacing 20% oxygen atoms ($\text{Li}_3\text{V}_2\text{O}_4\text{F}$). System 1 has fluorine at octahedral sites in a mixed cationic environment (FLi_3V_3 and FLi_4V_2) and system 2 in a lithium-segregated environment (FLi_6 and FLi_5V), as shown in Figure 4a and b, respectively. Table 1 lists the distortion mode coefficients of the two systems.

Figure 4 shows these configurations in relaxed positions and the corresponding pDOSs. Figure 4c exhibits that fluorine substitution increases the density of active cation states and stabilizes the nonbonding oxygen states by shifting them further below the Fermi level compared to the undoped case (Figure 3b). On the other hand, a greater suppression of anionic activity is shown by the structure in Figure 4b, where the fluorine atoms have eliminated all 2p oxygen states near the Fermi level, facilitating pure cationic redox over the charge transfer cycle (see pDOS in Figure 4d). This is the result of replacing nonbonding lone pairs of oxygen with the highly

electronegative pairs of fluorine, thereby burying these states deep in energy. One can observe an increased DOS of fluorine around -6 eV (Figure 4d) from the Fermi level, which is nowhere near active for redox. We have shown a similar comparison in a different disordered configuration (Figure S5) for repeatability.

Interestingly, structural distortion increases in the cation-mixed fluorine system (Figure 4a) as compared to the undoped case (22% jump in c norm), even though it stabilizes oxygen lone pairs. This is possibly due to the large electronegativity of fluorine attracting free lone pairs of 2p oxygen orbitals, producing irregularly mixed octahedrons. This might also be one of the reasons behind the severe capacity fade and structural degradation in $\text{Li}_2\text{VO}_2\text{F}$, assisting rapid O loss from the surface.²¹ In contrast, when these oxygen atoms with nonbonding electrons are replaced with fluorine (Figure 4b), the distortion is drastically reduced (59% and 66% drop in c norm with respect to undoped and cation-mixed fluorinated cases, respectively). All other distortion modes also show a similar drop in coefficients. In essence, the deliberate selection of fluorine-doping sites can subdue all anionic activity and prevent structural degradation accompanied by disorder. This property is crucial for mitigating hysteresis, ion migrations, and capacity fade over cycles, which have been attributed to anionic redox activity in TMOs.²⁰

Transition Metal Substitution. Transition metal substitution can help to facilitate or diminish anionic redox by either activating or stabilizing oxygen states near the Fermi level. The participation of the TM dopant in the redox process

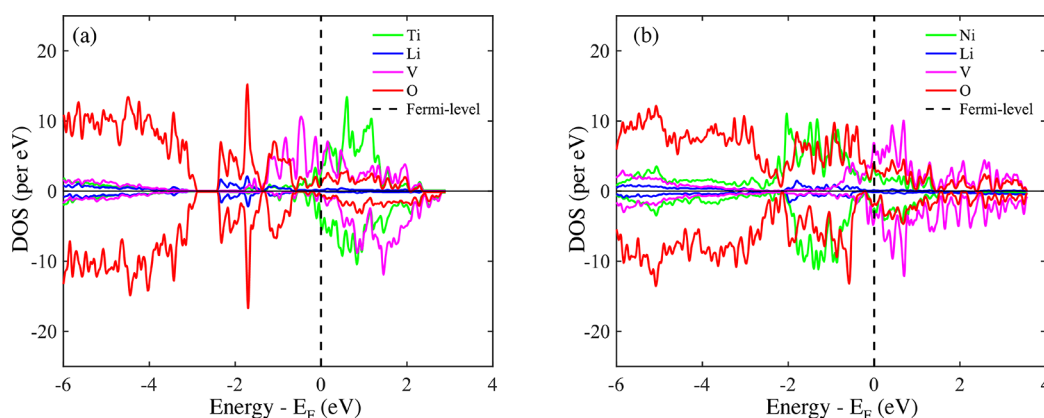


Figure 5. Effect of 50% cationic doping titanium (left) and nickel (right) on atom-projected DOS of disordered Li_3VTMO_5 . Titanium stabilizes oxygen nonbonding electrons and increases cation states in the conduction band, assisting cationic redox. In contrast, most nickel states are already filled, and nonbonding oxygen states are closer to the Fermi level, supporting anionic redox.

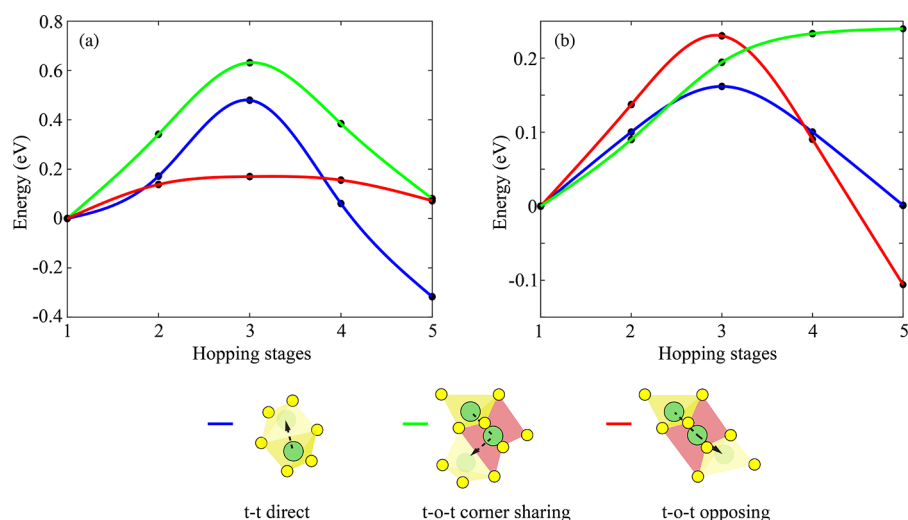


Figure 6. NEB migration barriers of the ordered (a) and disordered (b) configurations for the three lithium transition paths, direct t-t, corner sharing t-o-t, and opposing t-o-t. Only one path (opposing t-o-t) is feasible in the ordered system, while all paths become available in the disorder owing to a drastic drop in activation energy caused by weak covalent bonds. Opposing t-o-t can be spontaneously driven (0 meV). Barriers for the other two paths (150 and 230 meV, respectively) fall in the feasible range, being much smaller than that of graphite (420 meV).

will depend on the energy and hybridization of its 3d states with vanadium. Here we choose to substitute 50% of the vanadium atoms, so that all site configurations of the dopant have approximately the same average local environment in our $2 \times 2 \times 2$ supercell. As shown in Figure 5, the ratio of cationic vs anionic DOS above the Fermi level is lower in Ni as compared to Ti because they are mostly filled and inactive. Ni also pushes unhybridized oxygen states closer to the Fermi level, even though none of the other 3d metals activate the nonbonding 2p states above the Fermi level (Figure S4).

Similar to fluorine substitution at selected sites, structural distortion decreases with Ti doping, though it is small (4% drop in overall c norm as compared to the undoped case, Table 1) owing to weaker stabilization of oxygen states. Conversely, activation of oxygen states induced by Ni doping increases distortion, producing a significant jump of 40% in c norm. A part of this change is possibly due to a smaller size mismatch between Li and Ni ions (0.69 \AA ⁴⁶ vs 0.76 \AA ²³), which energetically opposes lithium segregation stemming from strong Coulombic repulsion. Further studies are required to assess behavior in other metrics like OCV, volume, and stress changes with TM doping.

Migration Barriers. Order-to-disorder transition is also accompanied by a change in diffusion properties. Macroscopic diffusion is more readily satisfied in Li-excess materials with long-distance connectivity of segregated OTM sites.^{23,24} $\text{Li}_3\text{V}_2\text{O}_5$ has 20% excess lithium ($x = 1.2$ in $\text{Li}_x\text{V}_{2-x}\text{O}_5$), which is higher than the threshold (9%) identified by Urban et al.²⁴ for activating long-distance percolation in DRS assuming only OTM lithium diffusion. Microscopic diffusion can be better quantified with migration barrier calculations for lithium transition from one stable site to another. Results of NEB calculations on pristine ($\text{Li}_3\text{V}_2\text{O}_5$) phases for two different configurations (most stable and least stable disorders) are shown in Figure 6. In the high-energy disorder, lithium diffusion through OTM sites is the predominant pathway.²⁴ The ordered structure does not have OTM sites, allowing primarily 1TM–1TM migration.

For these two systems, we have compared the three known lithium transition paths: direct t-t, corner-sharing t-o-t, and opposing t-o-t. Confirming previous studies,¹⁵ t-o-t opposing knock-off is the most favorable path (~ 150 meV) in ordered $\text{Li}_3\text{V}_2\text{O}_5$ owing to the least steric hindrance and Coulombic repulsion by vanadium atoms. Direct t-t and corner-sharing t-

o-t are at least 300 meV higher in activation energy. In the disordered system, however, all paths dramatically shift to lower energies; opposing t-o-t undergoes almost spontaneous transition (0 meV), while direct t-t (150 meV) and corner-sharing t-o-t (230 meV) paths are almost 50% less than lithium diffusion through the Frenkel mechanism in graphite (420 meV).⁴⁷ This should also shift the mass transport limit higher than that of graphite, providing more resistance against lithium plating.¹⁸ The crystal orbital Hamiltonian overlap (COHP) of summed V–O bonds in the disordered structure is also significantly smaller as compared to its counterpart (Figure S3). This indicates higher structural flexibility in the disordered system. Hence, higher distortion and weaker TM–O bonds facilitate easier lithium diffusion in the originally hindered migration paths. Consequently, all three paths get activated in the disordered system, leading to higher diffusion rates and faster charging ability.

CONCLUSIONS

We have quantified structural distortion and analyzed electronic structure and microscopic diffusion barriers in ordered and disordered $\text{Li}_3\text{V}_2\text{O}_5$, which is the delithiated starting point in the ω phase. The disorder is characterized by segregated lithium, weaker TM–O covalent bonds, disorganized octahedrons, and potentially redox-active oxygen states. In contrast, the ordered structure possesses mixed Li–V octahedrons with similar ionic radii, producing highly covalent TM–O bonds matching ideal octahedron geometry. The oxygen orbitals are delocalized and approach the O^{2-} state, as evidenced by the higher average electron population in its oxygen p orbitals. Using pDOS and COOP analysis, we can identify the positions of unhybridized oxygen 2p states and the associated changes in O–O bond strengths. At 0 K, these states are chemically inactive under high-energy disorder, which can get activated with voltage/temperature fluctuations. Additionally, we have found a positive trend between structural distortion and activation of anionic states using our first-principles analysis. This correlation is supported by anionic (fluorination) and cationic (3d metals) doping whereby replacement of selected oxygen sites significantly decreases distortion and anionic activity. We expect that this suppression of anionic activity will play an important role in reducing hysteresis and voltage fade in high-energy disorders.²⁰ In terms of lithium transport, higher energy disorders show better promise owing to their metallic character and structural flexibility. Lower TM–O bond strength and hindrance have reduced the activation energies of all 3D lithium hoppings, essential for fast charging.¹⁵ Hence, we encounter two effects from disorder-induced structural distortion in $\text{Li}_3\text{V}_2\text{O}_5$; it activates anionic states for potential redox and improves lithium transport.

It will be interesting to understand the effect of cationic and anionic doping on other performance metrics like OCV, volume and stress changes, migration barriers, etc., although these computations entail high computational cost. The problem could, however, be addressed by using state of the art machine-learning architectures as an alternative to DFT for high-throughput calculations. With novel Monte Carlo techniques, we can identify stable lithium intercalation sites and variation in disorder as a function of the charge state and report the on-the-fly convex hull of free energies and OCV.⁴⁸ One can also investigate other dopants like 4d and 5d metals and anions other than fluorine. Because layered V_2O_5 is a

popular cathode, an all-vanadate-based lithium-ion battery can be an important electrode combination to explore. Overall, our analysis should be relevant for experimentalists and theorists to further investigate the potential of doped disordered $\text{Li}_3\text{V}_2\text{O}_5$ as durable, fast-charging anodes. Owing to its low operational voltage (0.6 V), the present system with appropriate modifications is ideal for low-temperature and fast-charging applications, as it provides thermodynamic safety at weak kinetic conditions and faster lithium transport than graphite.

ASSOCIATED CONTENT

Supporting Information

The Supporting Information is available free of charge at <https://pubs.acs.org/doi/10.1021/acs.jpcc.2c03345>.

Summed COOP and COHP between O–O/V–O bonds in the disordered structure; electronic DOS for 3d-metal-substituted disordered systems other than Ti and Ni; filled out checklist (PDF)

AUTHOR INFORMATION

Corresponding Author

Venkatasubramanian Viswanathan – Mechanical Engineering Department, Carnegie Mellon University, Pittsburgh, Pennsylvania 15213, United States; orcid.org/0000-0003-1060-5495; Email: venkvis@cmu.edu

Authors

Mohammad Babar – Mechanical Engineering Department, Carnegie Mellon University, Pittsburgh, Pennsylvania 15213, United States; orcid.org/0000-0001-6779-3859

Hasnain Hafiz – Department of Physics, Northeastern University, Boston, Massachusetts 02115, United States

Zeeshan Ahmad – Pritzker School of Molecular Engineering, University of Chicago, Chicago, Illinois 60637, United States; orcid.org/0000-0001-9758-8952

Bernardo Barbiellini – Department of Physics, School of Engineering Science, LUT University, 53850 Lappeenranta, Finland; Department of Physics, Northeastern University, Boston, Massachusetts 02115, United States; orcid.org/0000-0002-3309-1362

Arun Bansil – Department of Physics, Northeastern University, Boston, Massachusetts 02115, United States

Complete contact information is available at: <https://pubs.acs.org/doi/10.1021/acs.jpcc.2c03345>

Notes

The authors declare no competing financial interest.

ACKNOWLEDGMENTS

We thank Dr. Zhuoying Zhu and Dr. Gus Hart for helpful discussions. M.B. and V.V. acknowledge support from the Office of Naval Research under Award No. N00014-19-1-2172. Acknowledgment is also made to the Extreme Science and Engineering Discovery Environment (XSEDE) for providing computational resources through Award No. TG-CTS180061. B.B. is supported by the Ministry of Education and Culture (Finland). A.B. acknowledges support by the US Department of Energy (DOE), Office of Science, Basic Energy Sciences grant number DE-FG02-07ER46352 and Northeastern University's Advanced Scientific Computation Center (ASCC) and the NERSC supercomputing center through DOE grant number DE-AC02-05CH11231.

REFERENCES

- (1) Choi, J. W.; Aurbach, D. Promise and reality of post-lithium-ion batteries with high energy densities. *Nat. Rev. Mater.* **2016**, *1*, 1–16.
- (2) Zeng, X.; Li, M.; Abd El-Hady, D.; Alshitari, W.; Al-Bogami, A. S.; Lu, J.; Amine, K. Commercialization of lithium battery technologies for electric vehicles. *Adv. Energy Mater.* **2019**, *9*, 1900161.
- (3) Zeng, X.; Zhan, C.; Lu, J.; Amine, K. Stabilization of a high-capacity and high-power nickel-based cathode for Li-ion batteries. *Chem.* **2018**, *4*, 690–704.
- (4) Chen, R.; Ren, S.; Knapp, M.; Wang, D.; Witter, R.; Fichtner, M.; Hahn, H. Disordered lithium-rich oxyfluoride as a stable host for enhanced Li⁺ intercalation storage. *Adv. Energy Mater.* **2015**, *5*, 1401814.
- (5) Yahia, M. B.; Vergnet, J.; Saubanère, M.; Doublet, M.-L. Unified picture of anionic redox in Li/Na-ion batteries. *Nat. Mater.* **2019**, *18*, 496–502.
- (6) Radin, M. D.; Vinckeviciute, J.; Seshadri, R.; Van der Ven, A. Manganese oxidation as the origin of the anomalous capacity of Mn-containing Li-excess cathode materials. *Nature Energy* **2019**, *4*, 639–646.
- (7) Yabuuchi, N.; Takeuchi, M.; Nakayama, M.; Shiiba, H.; Ogawa, M.; Nakayama, K.; Ohta, T.; Endo, D.; Ozaki, T.; Inamasu, T.; et al. High-capacity electrode materials for rechargeable lithium batteries: Li₃NbO₄-based system with cation-disordered rocksalt structure. *Proc. Natl. Acad. Sci. U. S. A.* **2015**, *112*, 7650–7655.
- (8) Whittingham, M. S. The role of ternary phases in cathode reactions. *J. Electrochem. Soc.* **1976**, *123*, 315.
- (9) Rocquefelte, X.; Boucher, F.; Gressier, P.; Ouvrard, G. First-Principle Study of the Intercalation Process in the Li_xV₂O₅ System. *Chemistry of materials* **2003**, *15*, 1812–1819.
- (10) Horrocks, G. A.; Likely, M. F.; Velazquez, J. M.; Banerjee, S. Finite size effects on the structural progression induced by lithiation of V₂O₅: a combined diffraction and Raman spectroscopy study. *Journal of Materials Chemistry A* **2013**, *1*, 15265–15277.
- (11) Pomerantseva, E.; Gerasopoulos, K.; Chen, X.; Rubloff, G.; Ghodssi, R. Electrochemical performance of the nanostructured biotemplated V₂O₅ cathode for lithium-ion batteries. *J. Power Sources* **2012**, *206*, 282–287.
- (12) Zhang, X.-F.; Wang, K.-X.; Wei, X.; Chen, J.-S. Carbon-coated V₂O₅ nanocrystals as high performance cathode material for lithium ion batteries. *Chem. Mater.* **2011**, *23*, S290–S292.
- (13) Wang, H.-g.; Ma, D.-l.; Huang, Y.; Zhang, X.-b. Electrospun V₂O₅ nanostructures with controllable morphology as high-performance cathode materials for lithium-ion batteries. *Chem.–Eur. J.* **2012**, *18*, 8987–8993.
- (14) Shepard, R.; Smeu, M. Ab initio investigation of α - and ζ -V₂O₅ for beyond lithium ion battery cathodes. *J. Power Sources* **2020**, *472*, 228096.
- (15) Liu, H.; Zhu, Z.; Yan, Q.; Yu, S.; He, X.; Chen, Y.; Zhang, R.; Ma, L.; Liu, T.; Li, M.; et al. A disordered rock salt anode for fast-charging lithium-ion batteries. *Nature* **2020**, *585*, 63–67.
- (16) Legrand, N.; Knosp, B.; Desprez, P.; Lapique, F.; Raël, S. Physical characterization of the charging process of a Li-ion battery and prediction of Li plating by electrochemical modelling. *J. Power Sources* **2014**, *245*, 208–216.
- (17) Verbrugge, M. W.; Koch, B. J. The effect of large negative potentials and overcharge on the electrochemical performance of lithiated carbon. *J. Electroanal. Chem.* **1997**, *436*, 1–7.
- (18) Petzl, M.; Kasper, M.; Danzer, M. A. Lithium plating in a commercial lithium-ion battery—A low-temperature aging study. *J. Power Sources* **2015**, *275*, 799–807.
- (19) Abdellahi, A.; Urban, A.; Dacek, S.; Ceder, G. The effect of cation disorder on the average Li intercalation voltage of transition-metal oxides. *Chem. Mater.* **2016**, *28*, 3659–3665.
- (20) Assat, G.; Tarascon, J.-M. Fundamental understanding and practical challenges of anionic redox activity in Li-ion batteries. *Nature Energy* **2018**, *3*, 373–386.
- (21) Clément, R.; Lun, Z.; Ceder, G. Cation-disordered rocksalt transition metal oxides and oxyfluorides for high energy lithium-ion cathodes. *Energy Environ. Sci.* **2020**, *13*, 345–373.
- (22) Lee, J.; Urban, A.; Li, X.; Su, D.; Hautier, G.; Ceder, G. Unlocking the potential of cation-disordered oxides for rechargeable lithium batteries. *science* **2014**, *343*, 519–522.
- (23) Ji, H.; Urban, A.; Kitchaev, D. A.; Kwon, D.-H.; Artrith, N.; Ophus, C.; Huang, W.; Cai, Z.; Shi, T.; Kim, J. C.; et al. Hidden structural and chemical order controls lithium transport in cation-disordered oxides for rechargeable batteries. *Nat. Commun.* **2019**, *10*, 1–9.
- (24) Urban, A.; Lee, J.; Ceder, G. The configurational space of rocksalt-type oxides for high-capacity lithium battery electrodes. *Adv. Energy Mater.* **2014**, *4*, 1400478.
- (25) Urban, A.; Abdellahi, A.; Dacek, S.; Artrith, N.; Ceder, G. Electronic-structure origin of cation disorder in transition-metal oxides. *Physical review letters* **2017**, *119*, 176402.
- (26) Giannozzi, P.; Baroni, S.; Bonini, N.; Calandra, M.; Car, R.; Cavazzoni, C.; Ceresoli, D.; Chiarotti, G. L.; Cococcioni, M.; Dabo, I.; et al. QUANTUM ESPRESSO: a modular and open-source software project for quantum simulations of materials. *J. Phys. Condens. Matter* **2009**, *21*, 395502.
- (27) Garrity, K. F.; Bennett, J. W.; Rabe, K. M.; Vanderbilt, D. Pseudopotentials for high-throughput DFT calculations. *Comput. Mater. Sci.* **2014**, *81*, 446–452.
- (28) Perdew, J. P.; Burke, K.; Ernzerhof, M. Generalized gradient approximation made simple. *Physical review letters* **1996**, *77*, 3865.
- (29) Du, Y.; Wang, X.; Sun, J. Tunable oxygen vacancy concentration in vanadium oxide as mass-produced cathode for aqueous zinc-ion batteries. *Nano Research* **2021**, *14*, 754–761.
- (30) Gani, T. Z.; Kulik, H. J. Where does the density localize? Convergent behavior for global hybrids, range separation, and DFT+U. *J. Chem. Theory Comput.* **2016**, *12*, S931–S945.
- (31) Scanlon, D. O.; Walsh, A.; Morgan, B. J.; Watson, G. W. An ab initio study of reduction of V₂O₅ through the formation of oxygen vacancies and Li intercalation. *J. Phys. Chem. C* **2008**, *112*, 9903–9911.
- (32) Jain, A.; Hautier, G.; Moore, C. J.; Ong, S. P.; Fischer, C. C.; Mueller, T.; Persson, K. A.; Ceder, G. A high-throughput infrastructure for density functional theory calculations. *Comput. Mater. Sci.* **2011**, *50*, 2295–2310.
- (33) Ling, C.; Zhang, R.; Mizuno, F. Phase stability and its impact on the electrochemical performance of VOPO₄ and LiVOPO₄. *Journal of Materials Chemistry A* **2014**, *2*, 12330–12339.
- (34) Fletcher, R. *Practical Methods of Optimization: Constrained Optimization*; John Wiley & Sons: New York, 1981; Vol. 2.
- (35) Maintz, S.; Deringer, V. L.; Tchougréeff, A. L.; Dronskowski, R. LOBSTER: A tool to extract chemical bonding from plane-wave based DFT. *J. Comput. Chem.* **2016**, *37*, 1030–1035.
- (36) Saubanère, M.; McCalla, E.; Tarascon, J.-M.; Doublet, M.-L. The intriguing question of anionic redox in high-energy density cathodes for Li-ion batteries. *Energy Environ. Sci.* **2016**, *9*, 984–991.
- (37) Hart, G. L.; Forcade, R. W. Algorithm for generating derivative structures. *Phys. Rev. B* **2008**, *77*, 224115.
- (38) Larsen, A. H.; Mortensen, J. J.; Blomqvist, J.; Castelli, I. E.; Christensen, R.; Dulak, M.; Friis, J.; Groves, M. N.; Hammer, B.; Hargus, C.; et al. The atomic simulation environment—a Python library for working with atoms. *J. Phys. Condens. Matter* **2017**, *29*, 273002.
- (39) Ong, S. P.; Richards, W. D.; Jain, A.; Hautier, G.; Kocher, M.; Cholia, S.; Gunter, D.; Chevrier, V. L.; Persson, K. A.; Ceder, G. Python Materials Genomics (pymatgen): A robust, open-source python library for materials analysis. *Comput. Mater. Sci.* **2013**, *68*, 314–319.
- (40) Jain, A.; Ong, S. P.; Hautier, G.; Chen, W.; Richards, W. D.; Dacek, S.; Cholia, S.; Gunter, D.; Skinner, D.; Ceder, G.; et al. Commentary: The Materials Project: A materials genome approach to accelerating materials innovation. *APL materials* **2013**, *1*, 011002.

- (41) Sarkar, A.; Velasco, L.; Wang, D.; Wang, Q.; Talasila, G.; de Biasi, L.; Kübel, C.; Brezesinski, T.; Bhattacharya, S. S.; Hahn, H.; et al. High entropy oxides for reversible energy storage. *Nat. Commun.* **2018**, *9*, 1–9.
- (42) Almessiere, M.; Slimani, Y.; El Sayed, H.; Baykal, A.; Ercan, I. Microstructural and magnetic investigation of vanadium-substituted Sr-nanohexaferrite. *J. Magn. Magn. Mater.* **2019**, *471*, 124–132.
- (43) Seo, D.-H.; Lee, J.; Urban, A.; Malik, R.; Kang, S.; Ceder, G. The structural and chemical origin of the oxygen redox activity in layered and cation-disordered Li-excess cathode materials. *Nat. Chem.* **2016**, *8*, 692–697.
- (44) Yu, D. Y. W.; Yanagida, K.; Kato, Y.; Nakamura, H. Electrochemical activities in Li₂MnO₃. *J. Electrochem. Soc.* **2009**, *156*, A417.
- (45) Kitchaev, D. A.; Lun, Z.; Richards, W. D.; Ji, H.; Clément, R. J.; Balasubramanian, M.; Kwon, D.-H.; Dai, K.; Papp, J. K.; Lei, T.; et al. Design principles for high transition metal capacity in disordered rocksalt Li-ion cathodes. *Energy Environ. Sci.* **2018**, *11*, 2159–2171.
- (46) Shannon, R. D. Revised effective ionic radii and systematic studies of interatomic distances in halides and chalcogenides. *Acta crystallographica section A: crystal physics, diffraction, theoretical and general crystallography* **1976**, *32*, 751–767.
- (47) Thinius, S.; Islam, M. M.; Heitjans, P.; Bredow, T. Theoretical study of Li migration in lithium–graphite intercalation compounds with dispersion-corrected DFT methods. *J. Phys. Chem. C* **2014**, *118*, 2273–2280.
- (48) Babar, M.; Parks, H. L.; Houchins, G.; Viswanathan, V. An accurate machine learning calculator for the lithium-graphite system. *J. Phys. Energy* **2021**, *3*, 014005.

Recommended by ACS

Doping-Induced Pre-Transformation to Extend Solid-Solution Regimes in Li-Ion Batteries

Parker Schofield, Sarbajit Banerjee, *et al.*

SEPTEMBER 06, 2022
ACS ENERGY LETTERS

READ 

Structural Characterization of the Delithiated Noncrystalline Phase in a Li-Rich Li₂VO₂F Cathode Material

Satoshi Hiroi, Osami Sakata, *et al.*

JULY 16, 2021
CHEMISTRY OF MATERIALS

READ 

Electrical Properties, Defect Structures, and Ionic Conducting Mechanisms in Alkali Tungstate Li₂W₂O₇

Jungu Xu, Kevin Huang, *et al.*

JUNE 02, 2021
INORGANIC CHEMISTRY

READ 

Atomistic Insights into the Effects of Doping and Vacancy Clustering on Li-Ion Conduction in the Li₃OCl Antiperovskite Solid Electrolyte

Matt J. Clarke, M. Saiful Islam, *et al.*

APRIL 20, 2021
ACS APPLIED ENERGY MATERIALS

READ 

Get More Suggestions >